Super-resolution imaging visualizes the eightfold symmetry of gp210 proteins around the nuclear pore complex and resolves the central channel with nanometer resolution

Anna Löschberger[1], Sebastian van de Linde[1], Marie-Christine Dabauvalle[2], Bernd Rieger[3], Mike Heilemann[1], Georg Krohne[2] and Markus Sauer[1,*]

[1]Department of Biotechnology and Biophysics, Biozentrum, Julius Maximilians University Würzburg, Am Hubland, 97074 Würzburg, Germany
[2]Department of Electron Microscopy, Biozentrum, Julius Maximilians University Würzburg, Am Hubland, 97074 Würzburg, Germany
[3]Department of Imaging Science and Technology, Delft University of Technology, Lorentzweg 1, 2628 CJ Delft, The Netherlands
*Author for correspondence (m.sauer@uni-wuerzburg.de)

Accepted 28 September 2011
Journal of Cell Science 125, 570–575

doi: 10.1242/jcs.098822

Summary

One of the most complex molecular machines of cells is the nuclear pore complex (NPC), which controls all trafficking of molecules in and out of the nucleus. Because of their importance for cellular processes such as gene expression and cytoskeleton organization, the structure of NPCs has been studied extensively during the last few decades, mainly by electron microscopy. We have used super-resolution imaging by direct stochastic optical reconstruction microscopy (*d*STORM) to investigate the structure of NPCs in isolated *Xenopus laevis* oocyte nuclear envelopes, with a lateral resolution of ~15 nm. By generating accumulated super-resolved images of hundreds of NPCs we determined the diameter of the central NPC channel to be 41±7 nm and demonstrate that the integral membrane protein gp210 is distributed in an eightfold radial symmetry. Two-color *d*STORM experiments emphasize the highly symmetric NPCs as ideal model structures to control the quality of corrections to chromatic aberration and to test the capability and reliability of super-resolution imaging methods.

Key words: Super-resolution imaging, Nuclear pore complex, dSTORM, Single-molecule localization

Introduction

The central role of nuclear pore complexes (NPCs) in nucleocytoplasmic transport has been extensively studied since their discovery in the 1950s (Callan and Tomlin, 1950; Gall, 1967). At the same time it has become evident that NPCs are not only simple gates but are also involved in regulatory processes on either side of the nuclear envelope (D'Angelo and Hetzer, 2008; Kahms et al., 2011; Strambio-De-Castillia et al., 2010). The structure of NPCs was elucidated by (cryo-) electron microscopy enabling the reconstruction of structural models with ~ 10 nm resolution (Beck et al., 2007; D'Angelo and Hetzer, 2008; Hinshaw and Milligan, 2003; Stoffler et al., 2003; Strambio-De-Castillia et al., 2010). NPCs are composed of multiple copies of at least 30 different proteins, called nucleoporins, which have a molecular mass of ~120 MDa in higher eukaryotes, i.e. they are among the largest molecular machines in the cell. NPCs are wheel-shaped, eightfold symmetrical cylindrical assemblies with an ~125 nm diameter core structure and a height of ~70 nm. They contain eight spokes arranged in a radially symmetrical fashion and a central channel with a diameter of 35–50 nm, as well as a cytoplasmic ring and a nuclear ring (Elad et al., 2009; Scheer et al., 2005; Strambio-De-Castillia et al., 2010). Filaments are attached to the cytoplasmic side and a basket structure to the nucleoplasmic side of the NPC.

Light microscopy is ideally suited to study cellular structures in a relatively non-invasive fashion. In particular, fluorescence microscopy is a valuable tool and is compatible with specific labeling protocols and live cell imaging. Owing to its sensitivity and high temporal resolution it has been used successfully to study dwell time durations of nuclear transport receptors (Dange et al., 2008), three-dimensional distribution of transient interactions in the NPC (Ma and Yang, 2010) and transport kinetics of single mRNA through NPCs (Grünwald and Singer, 2010). The spatial resolution of fluorescence microscopy is, however, limited to about half of the wavelength of light used to observe the sample (Abbe, 1873). Only recently, has the diffraction barrier been obviated by the introduction of so-called 'super-resolution imaging' methods that control the fluorescence emission of fluorescent probes in time using either deterministic approaches as in stimulated emission depletion microscopy (STED) (Klar et al., 2000) and structured illumination microscopy (SIM) (Gustafsson, 2000) or stochastic single-molecule localization approaches including photoactivated localization microscopy (PALM) (Betzig et al., 2006),

Journal of Cell Science

fluorescence photoactivation localization microscopy (FPALM) (Hess et al., 2006), stochastic optical reconstruction microscopy (STORM) (Rust et al., 2006), direct STORM (*d*STORM) (Heilemann et al., 2008; van de Linde et al., 2011) and other methods (Dertinger et al., 2009; Flors et al., 2007; Folling et al., 2008; Giannone et al., 2010; Lidke et al., 2005; Mizuno et al., 2011; Sharonov and Hochstrasser, 2006; Vogelsang et al., 2009). Recently, three-dimensional SIM was used to resolve single NPCs that colocalize with channels in the lamin network and peripheral heterochromatin but the resolution was too low to identify structural details of the NPC (Schermelleh et al., 2008).

We have used *d*STORM for super-resolution imaging of NPCs in nuclear envelopes isolated from *Xenopus laevis* oocytes. Reaching near-molecular resolution, *d*STORM is ideally suited to study the structural features of NPCs, which are known to have a symmetrical structure with a diameter well below the diffraction barrier and a high density of up to ~60 NPCs/μm^2 in mature *Xenopus laevis* oocytes (Spector, 1993). Furthermore, the highly symmetrical structure of NPCs makes it possible to reconstruct accumulated super-resolution images avoiding subjective selection processes ('cherry picking') and providing statistically confirmed super-resolution data.

Results and Discussion

For super-resolution imaging of NPCs we labeled gp210 proteins in the nuclear pore membrane indirectly by immunofluorescence using the primary antibody X222 directed against an epitope in the luminal side of gp210 (Gajewski et al., 1996) and Alexa Fluor 647 (Alexa647) secondary antibodies. Of the two integral membrane proteins, POM121 and gp210, identified so far only the latter is detectable in both animals and plants (Cohen et al., 2003). Evidence has been provided that gp210 is able to self-associate, forming homodimers that further associate into large arrays and it has been speculated that the dimers could form large circular multimers that surround and anchor the NPC on the luminal side of the pore membrane (Favreau et al., 2001). The established model requires the presence of at least eight dimers per NPC, which is compatible with the ~25 gp210 molecules estimated previously using conventional biochemical methods (Gerace et al., 1982).

*d*STORM images of NPCs reveal an eightfold symmetrical arrangement of gp210 proteins around NPCs (Fig. 1A–D, Fig. 2A–D and supplementary material Figs S1–S4). The resolved structures resemble, almost perfectly, the eightfold symmetrical ring structures seen by electron microscopy using negative staining (Fig. 1E). The isolation method used caused slight elongation of the nuclear envelopes so that they no longer appeared circular. Therefore, we selected NPCs that had a clear round appearance and calculated an average diameter for the eightfold symmetrical assembly of 161±17 nm (Fig. 2A,C).

To confirm statistically the eightfold symmetry, and demonstrate that the structures determined from the data are generally present in the *d*STORM data and not only in a selected subset (Fig. 2A–C) we generated accumulated super-resolution images (Fig. 3). We automatically detected possible pores from the *d*STORM image by template matching (Materials and Methods and supplementary material Figs S5–S7) and combined all identified 426 individual rings into one combined super-resolved image by rotation alignment (Fig. 3A). Analysis of the average super-resolution image revealed a perfect eightfold symmetry of the gp210 ring with a diameter of 164±7 nm (Fig. 3A).

To assess the width of the central channel of NPCs we used fluorescently labeled wheat germ agglutinin (WGA) binding to *N*-acetylglucosamine-modified nucleoporins (Fig. 2; supplementary material Fig. S3) (Cordes et al., 1991; Davis and Blobel, 1987). Because of small differences in labeling efficiency caused by steric hindrance or accessibility of epitopes the homogeneity of the fluorescent ring structures varies, especially in the narrow central channel (Fig. 2; supplementary material Fig. S3). Nevertheless, we could clearly resolve the central channel with a diameter of 35–50 nm in individual NPCs (Fig. 2B,C; Fig. 4). This was possible because we used the bright photoswitchable fluorophore Alexa647, which can be detected with nanometer precision (Smith et al., 2010). We determined the spatial resolution of WGA–Alexa647 in the central channel of 50 different NPCs from the full width at half maximum (FWHM) of the *d*STORM images to be 15±4 nm (Fig. 2D). From the subpopulation of selected ring structures we determined the diameter of the central channel to be 38±5 nm (Fig. 2D).

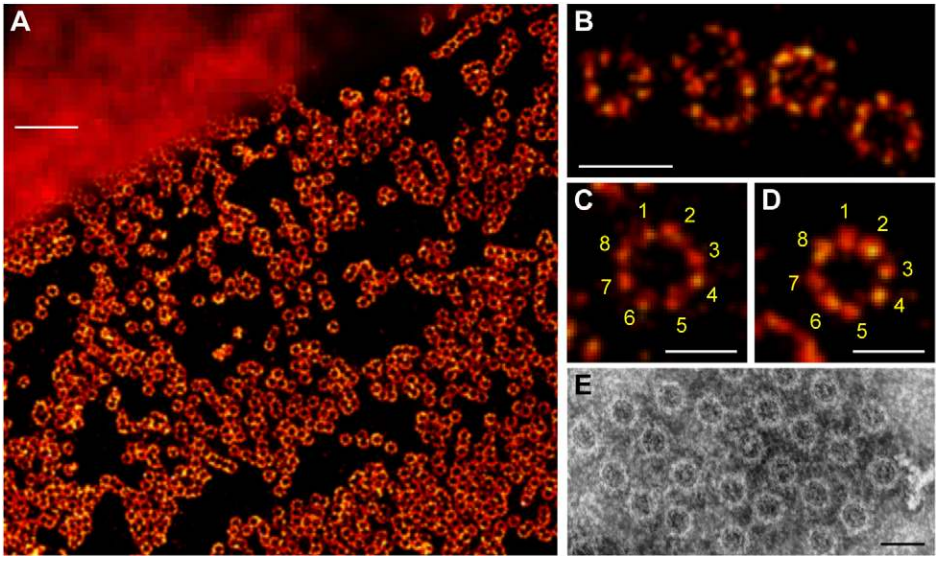

Fig. 1. *d*STORM of the NPC integral membrane protein gp210. (**A**) Comparison of widefield fluorescence (upper left corner) and *d*STORM image (lower right corner). gp210 proteins in nuclear envelopes isolated from *Xenopus laevis* oocytes were labeled by indirect immunofluorescence using the primary antibody X222 directed against an epitope located in the lumen of the nuclear envelope bordering the pore wall (Gajewski et al., 1996) and Alexa647 secondary antibodies. (**B**–**D**) Higher magnifications of fluorescent circular structures to highlight the eightfold symmetrical arrangement of gp210 proteins in NPCs. (**E**) NPCs are generally seen as eightfold symmetrical ring structures in electron microscopy using negative staining. Scale bars: 1 μm (A), 250 nm (B), 150 nm (C–E).

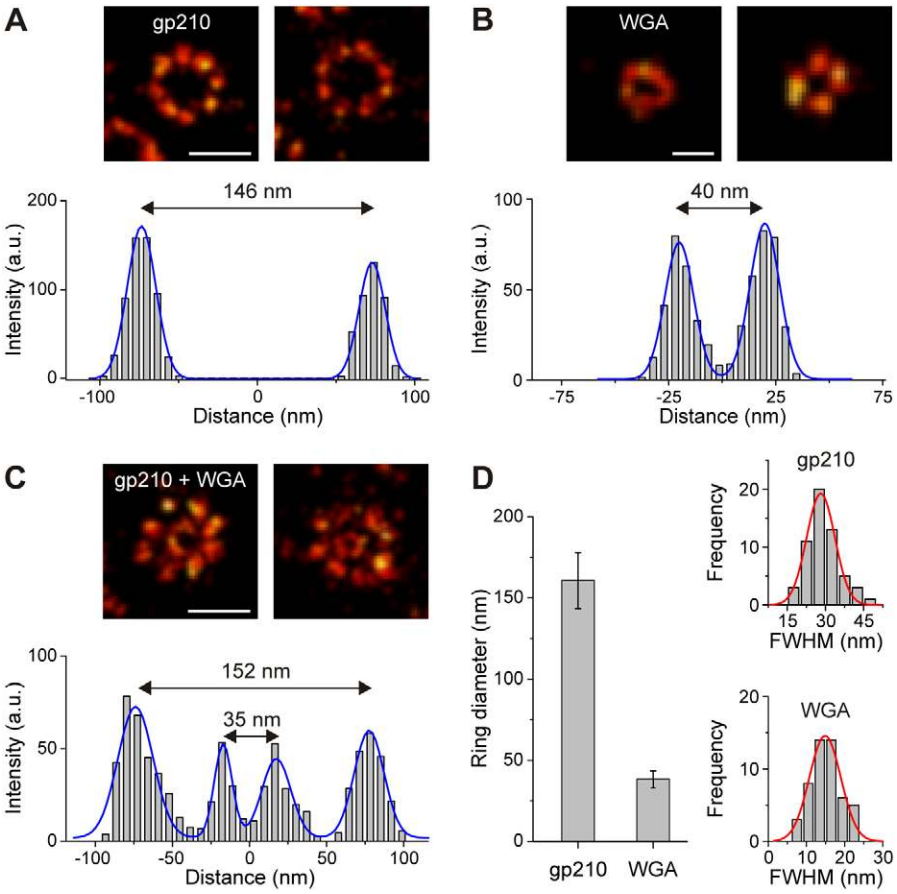

Fig. 2. Distribution of gp210 and WGA in NPCs as revealed by *d*STORM. In each case two representative examples are shown to emphasize differences in labeling efficiency. (**A**) The integral membrane protein gp210 surrounding the NPC labeled by immunofluorescence with Alexa647. The cross-section profile (below) of the left ring structure yields a ring diameter of 146 nm. (**B**) Nucleoporins of the central channel labeled with WGA–Alexa647. The cross-section profile of the left image yields a channel diameter of 40 nm. (**C**) Diameters were confirmed by double staining of gp210 and WGA-binding nucleoporins located in the central channel of the NPC. Here diameters of 152 and 35 nm were calculated from a cross-section profile of the left image for the outer and the inner ring, respectively. (**D**) Average values of outer ring and central channel diameters as calculated from 50 different NPC ring structures. The diameter of the gp210 ring structure was determined as 161±17 nm , and the diameter of the central channel to be 38±5 nm. In addition, the distribution of FWHM values extracted from the cross-sectional profiles for gp210 and WGA showed the FWHM to be 29±7 nm for gp210 and 15±4 nm for WGA. Scale bars: 150 nm (A,C) 50 nm (B).

The accumulated super-resolution images of 621 small rings of the central channel reveal an inner diameter of 41±7 nm, a value that agrees very well with previous findings (Fig. 3B) (Elad et al., 2009; Scheer et al., 2005; Strambio-De-Castillia et al., 2010). Considering the molecular size of a the WGA dimer of ~5 nm (Schwefel et al., 2010) and random fluorophore labeling, the diameter of the central NPC channel appears to be surprisingly consistent. Owing to the large molecular size of gp210 (200 kDa) (Favreau et al., 2001) and the fact that we used IgG antibodies and $F(ab')_2$ fragments for indirect labeling with molecular sizes of 8–10 nm, the exact size of the NPC-anchoring gp210 proteins was difficult to determine. Therefore, we cannot explicitly distinguish between gp210 monomers and dimers. However, our data suggest that gp210 proteins are organized by interactions with the pore complex core octamer and support the model in which eight gp210 dimers are present for anchoring the NPC (Fig. 1B–D; Figs 2, 3) (Favreau et al., 2001; Gerace et al., 1982).

Double-staining experiments with identical (Alexa647) and different (Alexa647 and ATTO520) fluorophores revealed similar structures: gp210 proteins form an eightfold symmetrical ring arranged around NPCs with a central smaller ring (Fig. 2C; Figs 3, 4; supplementary material Fig. S4).

Using both the gp210 and WGA *d*STORM data (Figs 1, 4; supplementary material Figs S1–S3) we calculated a NPC density of 9–24 NPCs/μm^2 for different *Xenopus laevis* oocyte nuclear envelope preparations. The fact that the circular fluorescence assemblies in *d*STORM images show an eightfold perfectly symmetrical gp210 ring around each NPC and a substantially smaller central ring (Fig. 2C, Fig. 4; supplementary material Figs S1–S4) demonstrates a high binding specificity of the X222 antibody to gp210 proteins and WGA at nucleoporins in the central channel of the NPC. Our results underscore the ability of *d*STORM in combination with refined data analysis to resolve complex molecular structures with an optical resolution well below 20 nm. For the first time, we could resolve the eightfold symmetry of the gp210 ring around each NPC and determine the diameter of the central channel with nanometer accuracy using light microscopy. Furthermore, we show that NPCs can serve as

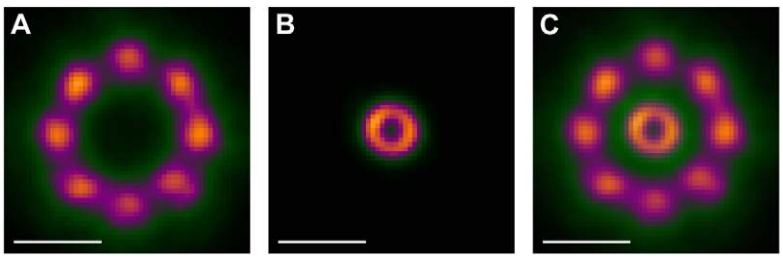

Fig. 3. Image analysis of accumulated NPC *d*STORM data. (**A**) For gp210, 426 individual rings containing ~160,000 localizations were combined to yield an average diameter of 164±7 nm for the gp210 ring surrounding the NPC. (**B**) For WGA, 621 rings containing ~40,000 localizations were combined and a diameter of 41±7 nm was determined for the central channel of the NPC. (**C**) Superimposed image of both structures. Scale bars: 100 nm.

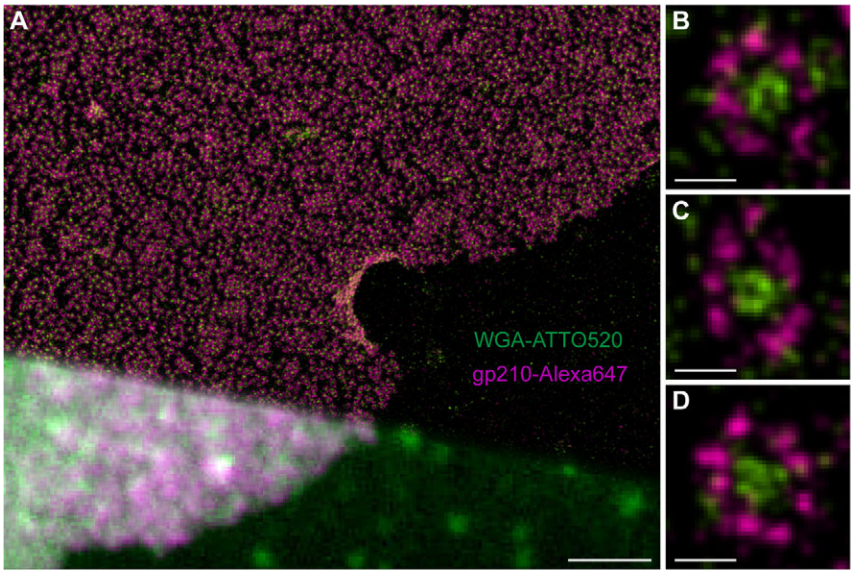

Fig. 4. Two-color *d*STORM images of NPCs using WGA-ATTO520 and Alexa647-labeled secondary antibodies directed against an epitope of gp210 on the luminal side. (**A**) Comparison of conventional widefield fluorescence image (lower left corner) and *d*STORM image (upper right corner). (**B**–**D**) Higher magnification reveals the typical eightfold symmetrical ring structure of gp210 proteins (violet) surrounding the NPC and *N*-acetyl glucosamine-containing nucleoporins in the central channel labeled with WGA-ATTO520 (green). Scale bars: 2.5 µm (A), 100 nm (B–D).

model structures to demonstrate the capability and reliability of super-resolution imaging methods. Additionally, NPCs are ideally suited to control the efficiency of chromatic aberration corrections in multicolor super-resolution imaging experiments (Fig. 4; supplementary material Fig. S8).

Our results emphasize the remarkable optical resolution that stochastic single-molecule based super-resolution imaging methods can achieve using standard, commercially available fluorescent probes. We envisage that live-cell *d*STORM (Klein et.al., 2011; van de Linde et al., 2011; Wombacher et al., 2010) in combination with single-molecule tracking (Grünwald and Singer, 2010) could pave the way towards NPC functional imaging with previously unmatched spatiotemporal resolution.

Materials and Methods

Materials

Xenopus laevis were purchased from Xenopus Express (Vernassai, France) and kept in tanks of water at 20°C. Mouse monoclonal antibodies X222 and Asc222a2 directed against gp210 were provided by Georg Krohne (Gajewski et al., 1996). Alexa647-conjugated F(ab′)2 fragments of goat anti-mouse-IgG (A-21237) and Alexa647-conjugated wheat germ agglutinin (W32466), were purchased from Invitrogen. WGA (lectin from *Triticum vulgaris*) was from Sigma-Aldrich (L9640) and ATTO520 *N*-hydroxysuccinimidyl ester from ATTO-TEC (Siegen, Germany; AD 520).

Manual isolation and fixation of nuclear envelopes

Small pieces of ovaries were removed from anesthetized animals and placed in modified Barth's medium (Gurdon, 1976). After manual removal of the follicle epithelium, oocytes were transferred in '3:1 medium' (75 mM KCl, 25 mM NaCl, Tris-HCl, pH 7.2) and the nuclei were manually isolated as described elsewhere (Krohne et al., 1978). Briefly, an oocyte was torn open in 3:1 medium and the released nucleus was cleaned of yolk and other cytoplasmic contaminants by repeated sucking up and down in a narrow-bore pipette. The nucleus was then transferred into a Lab-Tek II chambered coverglass containing 3:1 medium. With a pair of no. 5 Dumont forceps the nuclear envelope was opened and spread on the coverglass. In this condition, with the nuclear envelope attached to the coverglass, the nuclear contents pop out of the envelope. The nuclear envelope was then washed twice in 3:1 medium and fixed for 20 minutes with 2% paraformaldehyde in phosphate-buffered saline (PBS; supplementary material Fig. S1).

Immunofluorescence and WGA labeling

The spread nuclear envelopes were washed in PBS and saturated with 0.5% bovine serum albumin (BSA; Serva) in PBS for 10 minutes. After incubation with X222 antibodies for 45 minutes, the nuclear envelope was washed for 10 minutes in PBS, followed by a second incubation step with Alexa647 $F(ab')_2$ fragments of goat anti-mouse IgG for 30 minutes and a final washing step for 20 minutes. For double staining of gp210 and *N*-acetylglucosamine-modified nucleoporins of the central channel, a third incubation step was performed using custom-labeled WGA-ATTO520 with a washing step in between. Staining was performed by incubating the sample for 10 minutes with 5 µg/µl WGA–ATTO520. Before *d*STORM imaging, the sample was incubated in 2% paraformaldehyde in PBS for 5 minutes. Samples were stored in PBS with 0.2% sodium azide. The degree of labeling (DOL) with Alexa647-labeled antibodies was determined to ~4. WGA was labeled with ATTO520 according to standard coupling protocols given by the supplier. The conjugates were purified on NAP-5 filtration columns (Sephadex G-25 DNA Grade, GE Healthcare). The DOL of WGA–ATTO520 was determined to 0.5–1.0.

Photoswitching buffer

Reversible photoswitching of Alexa647 and ATTO520 was performed in 100 mM β-mercaptoethylamine (MEA; Sigma) in PBS, pH 7.4–8.0, applying an oxygen scavenger system [0.5 mg/ml glucose oxidase (Sigma), 40 µg/ml catalase (Sigma), 10% w/v glucose] (van de Linde et al., 2011).

Electron microscopy

Electron micrographs of negatively stained nuclear envelopes of *X. laevis* oocytes were taken as described by Krohne et al. (Krohne et al., 1978).

Super-resolution imaging

*d*STORM was performed as described elsewhere (van de Linde et al., 2011), using an inverted microscope (Olympus IX-71) equipped with an oil-immersion objective (×60, NA 1.45; Olympus). A 641 nm diode laser (Cube 640–100C, Coherent, Santa Clara, CA) was used for excitation of Alexa647, and a 488 nm laser (Sapphire 488LP; Coherent) was used for excitation of ATTO520. A polychromatic mirror (HC 410/504/582/669; Semrock, Rochester, NY) was used to separate laser and fluorescence light; the latter was imaged on an electron-multiplying CCD (EMCCD; Ixon DU897, Andor) camera. Additional band pass filters were used in the detection path of the setup (ET700/75, HQ535/50; Chroma). Additional lenses were used to achieve a final camera pixel size of 105 nm. 20,000–30,000 frames were recorded with frame rates of 100–140 Hz at irradiation intensities of 1–5 kW/cm^2.

Image reconstruction and data analysis

*d*STORM images were reconstructed and analyzed with the open source software rapidSTORM 1.4.11 (Wolter et al., 2010). Only fluorescent spots containing more than 500 photons (ATTO520) and more than 1000 photons (Alexa647) were analyzed. By analyzing their ellipticity, multi-fluorophore events were discarded from further analysis (Wolter et al., 2011). Typically, 1000 photons were detected per ATTO520 molecule and frame, whereas 3500 photons were detected per Alexa647 molecule and frame. The structure shown in Fig. 4A was reconstructed from ~371,000 localizations of ATTO520 and ~1,290,000 localizations of Alexa647. Reconstructed images were convolved with a Gaussian function with a standard deviation of 1 pixel (supplementary material Fig. S9) using ImageJ (Abramoff, 2004). Distance measurements as shown in Fig. 2A–C were performed with unprocessed data. Overviews of *d*STORM images are shown with a grid of 15–20 nm pixel size, whereas detailed images are shown with a grid of 5–7 nm

pixel size. To determine the diameter of the gp210 ring structure, cross-section profiles were made through the center of the ring. The intensity distribution along the profile was fitted with a model of a double Gaussian function, where the difference of both centroids represents the diameter of the ring (Fig. 2A). The diameter of *N*-acetylglucosamine-modified nucleoporins of the central channel was determined in the same way (Fig. 2B). The FWHM of each Gaussian function was calculated to determine the optical resolution in the lateral direction. Data from double stained NPCs were analyzed by fitting a quadruple Gaussian model function (Fig. 2C). The average diameter and FWHM of gp210 and WGA were determined from different NPCs. Error bars in Fig. 2D represent the standard deviation of 25–28 and 50–56 measurements to determine the diameter and the FWHM, respectively.

Average image analysis

To show that the structures that were determined are generally present and not just found in a selected subset of the data, we combined individual pores into one 'average' pore to increase the number of detections per image. To this end we automatically detected possible pores from the super-resolution image (supplementary material Fig. S5) by template matching using DIPimage (www.diplib.org) and Matlab (Mathworks). For all possible pores a model was fitted to the detected localizations: either an eightfold ring (gp210-labeled images) or just a ring (WGA-labeled images). As a cost function we optimized the sum of the distances from the detected localizations to the closest model point. All localizations were then aligned by shift and/or rotation, based on the fit parameters, and combined into one image (Fig. 3). For gp210 we combined ~160,000 detected localizations in 426 individual rings and estimated a diameter of 164±7 nm, and for WGA, we combined ~40,000 detected localizations in 621 rings, and estimated a diameter of 41±7 nm (means ± standard deviations). The radius of the combined ring was estimated from its angular average (supplementary material Figs S6, S7). The peak of this average can be estimated very precisely because of the very large number of localizations, however, the peak position has to be corrected (van Vliet and Verbeek, 1994). The correction is $-0.5s^2/R^2$, where s is the standard deviation of the distribution and R is the peak position.

Two-color imaging and image alignment

Dual-color imaging was performed by imaging Alexa647 and ATTO520 sequentially. Alexa647 was imaged first to prevent photobleaching. To correct shifts due to chromatic aberrations, usually both channels are aligned by using multifluorescent beads. By determining the vector field, one image is transformed to fit the other image. In the case of dual-labeled NPC proteins, the highly symmetrical nature of the structure can be used for intrinsic alignment. Therefore, the center of gp210 and WGA ring structures that clearly belong to each other were identified manually and used as reference points. Thereby several reference points in different parts of the image were used for transformation of the red (Alexa647) channel image using ImageJ (bUnwapJ) (Arganda-Carreras et al., 2006) (supplementary material Fig. S8).

Acknowledgements

We thank U. Scheer for helpful discussions.

Funding

This work was supported by the Biophoptonics Initiative of the Bundesministerium für Bildung und Forschung [13N11019 to M.S. and FKZ 0315262 to M.H.]. Deposited in PMC for immediate release.

Supplementary material available online at
http://jcs.biologists.org/lookup/suppl/doi:10.1242/jcs.098822/-/DC1

References

Abbe, E. (1873). Theorie des Mikroskops und der mikroskopischen Wahrnehmung. *Arch. Mikrosk. Anat.* **9**, 413-420.

Abramoff, M. D., Magelhaes, P. J. and Ram, S. J. (2004). Image processing with ImageJ. *Biophotonics Int.* **11**, 36-42.

Arganda-Carreras, I., Sánchez Sorzano, C. Ó., Marabini, R., Carazo, J. M., Ortiz-de Solorzano, C. and Kybic, J. (2006). Consistent and elastic registration of histological sections using vector-spline regularization. *Lect. Notes Comput. Sci.* **4241**, 85-95.

Beck, M., Lucic, V., Forster, F., Baumeister, W. and Medalia, O. (2007). Snapshots of nuclear pore complexes in action captured by cryo-electron tomography. *Nature* **449**, 611-615.

Betzig, E., Patterson, G. H., Sougrat, R., Lindwasser, O. W., Olenych, S., Bonifacino, J. S., Davidson, M. W., Lippincott-Schwartz, J. and Hess, H. F. (2006). Imaging intracellular fluorescent proteins at nanometer resolution. *Science* **313**, 1642-1645.

Callan, H. G. and Tomlin, S. G. (1950). Experimental studies on amphibian oocyte nuclei. I. Investigation of the structure of the nuclear membrane by means of the electron microscope. *Proc. R. Soc. B* **137**, 367-378.

Cohen, M., Feinstein, N., Wilson, K. L. and Gruenbaum, Y. (2003). Nuclear pore protein gp210 is essential for viability in HeLa cells and Caenorhabditis elegans. *Mol. Biol. Cell* **14**, 4230-4237.

Cordes, V., Waizenegger, I. and Krohne, G. (1991). Nuclear pore complex glycoprotein p62 of Xenopus laevis and mouse: cDNA cloning and identification of its glycosylated region. *Eur. J. Cell Biol.* **55**, 31-47.

D'Angelo, M. A. and Hetzer, M. W. (2008). Structure, dynamics and function of nuclear pore complexes. *Trends Cell Biol.* **18**, 456-466.

Dange, T., Grunwald, D., Grunwald, A., Peters, R. and Kubitscheck, U. (2008). Autonomy and robustness of translocation through the nuclear pore complex: a single-molecule study. *J. Cell Biol.* **183**, 77-86.

Davis, L. I. and Blobel, G. (1987). Nuclear pore complex contains a family of glycoproteins that includes p62: glycosylation through a previously unidentified cellular pathway. *Proc. Natl. Acad. Sci. USA* **84**, 7552-7556.

Dertinger, T., Colyer, R., Iyer, G., Weiss, S. and Enderlein, J. (2009). Fast, background-free, 3D super-resolution optical fluctuation imaging (SOFI). *Proc. Natl. Acad. Sci. USA* **106**, 22287-22292.

Elad, N., Maimon, T., Frenkiel-Krispin, D., Lim, R. Y. and Medalia, O. (2009). Structural analysis of the nuclear pore complex by integrated approaches. *Curr. Opin. Struct. Biol.* **19**, 226-232.

Favreau, C., Bastos, R., Cartaud, J., Courvalin, J. C. and Mustonen, P. (2001). Biochemical characterization of nuclear pore complex protein gp210 oligomers. *Eur. J. Biochem.* **268**, 3883-3889.

Flors, C., Hotta, J., Uji-i, H., Dedecker, P., Ando, R., Mizuno, H., Miyawaki, A. and Hofkens, J. (2007). A stroboscopic approach for fast photoactivation-localization microscopy with Dronpa mutants. *J. Am. Chem. Soc.* **129**, 13970-13977.

Folling, J., Bossi, M., Bock, H., Medda, R., Wurm, C. A., Hein, B., Jakobs, S., Eggeling, C. and Hell, S. W. (2008). Fluorescence nanoscopy by ground-state depletion and single-molecule return. *Nat. Methods* **5**, 943-945.

Gajewski, A., Lourim, D. and Krohne, G. (1996). An antibody against a glycosylated integral membrane protein of the Xenopus laevis nuclear pore complex: a tool for the study of pore complex membranes. *Eur. J. Cell Biol.* **71**, 14-21.

Gall, J. G. (1967). Octagonal nuclear pores. *J. Cell Biol.* **32**, 391-399.

Gerace, L., Ottaviano, Y. and Kondor-Koch, C. (1982). Identification of a major polypeptide of the nuclear pore complex. *J. Cell Biol.* **95**, 826-837.

Giannone, G., Hosy, E., Levet, F., Constals, A., Schulze, K., Sobolevsky, A. I., Rosconi, M. P., Gouaux, E., Tampe, R., Choquet, D. et al. (2010). Dynamic superresolution imaging of endogenous proteins on living cells at ultra-high density. *Biophys. J.* **99**, 1303-1310.

Grünwald, D. and Singer, R. H. (2010). In vivo imaging of labelled endogenous beta-actin mRNA during nucleocytoplasmic transport. *Nature* **467**, 604-607.

Gurdon, J. B. (1976). Injected nuclei in frog oocytes: fate, enlargement, and chromatin dispersal. *J. Embryol. Exp. Morphol.* **36**, 523-540.

Gustafsson, M. G. (2000). Surpassing the lateral resolution limit by a factor of two using structured illumination microscopy. *J. Microsc.* **198**, 82-87.

Heilemann, M., van de Linde, S., Schuttpelz, M., Kasper, R., Seefeldt, B., Mukherjee, A., Tinnefeld, P. and Sauer, M. (2008). Subdiffraction-resolution fluorescence imaging with conventional fluorescent probes. *Angew. Chem. Int. Ed. Engl.* **47**, 6172-6176.

Hess, S. T., Girirajan, T. P. and Mason, M. D. (2006). Ultra-high resolution imaging by fluorescence photoactivation localization microscopy. *Biophys. J.* **91**, 4258-4272.

Hinshaw, J. E. and Milligan, R. A. (2003). Nuclear pore complexes exceeding eightfold rotational symmetry. *J. Struct. Biol.* **141**, 259-268.

Kahms, M., Huve, J., Wesselmann, R., Farr, J. C., Baumgartel, V. and Peters, R. (2011). Lighting up the nuclear pore complex. *Eur. J. Cell Biol.* **90**, 751-758.

Klar, T. A., Jakobs, S., Dyba, M., Egner, A. and Hell, S. W. (2000). Fluorescence microscopy with diffraction resolution barrier broken by stimulated emission. *Proc. Natl. Acad. Sci. USA* **97**, 8206-8210.

Klein, T., Loschberger, A., Proppert, S., Wolter, S., van de Linde, S. and Sauer, M. (2011). Live-cell dSTORM with SNAP-tag fusion proteins. *Nat. Methods* **8**, 7-9.

Krohne, G., Franke, W. W. and Scheer, U. (1978). The major polypeptides of the nuclear pore complex. *Exp. Cell Res.* **116**, 85-102.

Lidke, K., Rieger, B., Jovin, T. and Heintzmann, R. (2005). Superresolution by localization of quantum dots using blinking statistics. *Opt. Express* **13**, 7052-7062.

Ma, J. and Yang, W. (2010). Three-dimensional distribution of transient interactions in the nuclear pore complex obtained from single-molecule snapshots. *Proc. Natl. Acad. Sci. USA* **107**, 7305-7310.

Mizuno, H., Abe, M., Dedecker, P., Makino, A., Rocha, S., Ohno-Iwashita, Y., Hofkens, J., Kobayashi, T. and Miyawaki, A. (2011). Fluorescent probes for superresolution imaging of lipid domains on the plasma membrane. *Chem. Sci.* **2**, 1548-1553.

Rust, M. J., Bates, M. and Zhuang, X. (2006). Sub-diffraction-limit imaging by stochastic optical reconstruction microscopy (STORM). *Nat. Methods* **3**, 793-795.

Scheer, U., Dabauvalle, M. C., Krohne, G., Peiman Zahedi, R. and Sickmann, A. (2005). Nuclear envelopes from amphibian oocytes--from morphology to protein inventory. *Eur. J. Cell Biol.* **84**, 151-162.

Schermelleh, L., Carlton, P. M., Haase, S., Shao, L., Winoto, L., Kner, P., Burke, B., Cardoso, M. C., Agard, D. A., Gustafsson, M. G. et al. (2008). Subdiffraction multicolor imaging of the nuclear periphery with 3D structured illumination microscopy. *Science* **320**, 1332-1336.

Schwefel, D., Maierhofer, C., Beck, J. G., Seeberger, S., Diederichs, K., Moller, H. M., Welte, W. and Wittmann, V. (2010). Structural basis of multivalent binding to wheat germ agglutinin. *J. Am. Chem. Soc.* **132**, 8704-8719.

Sharonov, A. and Hochstrasser, R. M. (2006). Wide-field subdiffraction imaging by accumulated binding of diffusing probes. *Proc. Natl. Acad. Sci. USA* **103**, 18911-18916.

Smith, C. S., Joseph, N., Rieger, B. and Lidke, K. A. (2010). Fast, single-molecule localization that achieves theoretically minimum uncertainty. *Nat. Methods* **7**, 373-375.

Spector, D. L. (1993). Macromolecular domains within the cell nucleus. *Annu. Rev. Cell Biol.* **9**, 265-315.

Stoffler, D., Feja, B., Fahrenkrog, B., Walz, J., Typke, D. and Aebi, U. (2003). Cryo-electron tomography provides novel insights into nuclear pore architecture: implications for nucleocytoplasmic transport. *J. Mol. Biol.* **328**, 119-130.

Strambio-De-Castillia, C., Niepel, M. and Rout, M. P. (2010). The nuclear pore complex: bridging nuclear transport and gene regulation. *Nat. Rev. Mol. Cell Biol.* **11**, 490-501.

van de Linde, S., Loschberger, A., Klein, T., Heidbreder, M., Wolter, S., Heilemann, M. and Sauer, M. (2011). Direct stochastic optical reconstruction microscopy with standard fluorescent probes. *Nat. Protoc.* **6**, 991-1009.

van Vliet, L. J. and Verbeek, P. W. (1994). Edge localization by MoG filters: Multiple-of-Gaussians. *Pattern Recognit. Lett.* **15**, 485-496.

Vogelsang, J., Cordes, T., Forthmann, C., Steinhauer, C. and Tinnefeld, P. (2009). Controlling the fluorescence of ordinary oxazine dyes for single-molecule switching and superresolution microscopy. *Proc. Natl. Acad. Sci. USA* **106**, 8107-8112.

Wolter, S., Schuttpelz, M., Tscherepanow, M., van de Linde, S., Heilemann, M. and Sauer, M. (2010). Real-time computation of subdiffraction-resolution fluorescence images. *J. Microsc.* **237**, 12-22.

Wolter, S., Endesfelder, U., van de Linde, S., Heilemann, M. and Sauer, M. (2011). Measuring localization performance of super-resolution algorithms on very active samples. *Opt. Express* **19**, 7020-7033.

Wombacher, R., Heidbreder, M., van de Linde, S., Sheetz, M. P., Heilemann, M., Cornish, V. W. and Sauer, M. (2010). Live-cell super-resolution imaging with trimethoprim conjugates. *Nat. Methods* **7**, 717-719.

Journal of Cell Science